Lattice-Boltzmann Modelling of Internal Compressible Flows: Application to the Transonic LS89 Cascade

Iason Tsetoglou, Song Zhao, Jérôme Jacob, Pierre Boivin

▶ **To cite this version:**

Iason Tsetoglou, Song Zhao, Jérôme Jacob, Pierre Boivin. Lattice-Boltzmann Modelling of Internal Compressible Flows: Application to the Transonic LS89 Cascade. Proceedings of the ASME Turbo Expo 2024: Turbomachinery Technical Conference and Exposition, Jun 2024, London, United Kingdom. 10.1115/GT2024-123051 . hal-04731567

HAL Id: hal-04731567
https://hal.science/hal-04731567v1

Submitted on 11 Oct 2024

HAL is a multi-disciplinary open access archive for the deposit and dissemination of scientific research documents, whether they are published or not. The documents may come from teaching and research institutions in France or abroad, or from public or private research centers.

L'archive ouverte pluridisciplinaire **HAL**, est destinée au dépôt et à la diffusion de documents scientifiques de niveau recherche, publiés ou non, émanant des établissements d'enseignement et de recherche français ou étrangers, des laboratoires publics ou privés.

Tsetoglou, I, Zhao, S, Jacob, J, Boivin, P. "Lattice-Boltzmann Modelling of Internal Compressible Flows: Application to the Transonic LS89 Cascade." Proceedings of the ASME Turbo Expo 2024: Turbomachinery Technical Conference and Exposition. Volume 12C: Turbomachinery — Design Methods and CFD Modeling for Turbomachinery; Ducts, Noise, and Component Interactions. London, United Kingdom. June 24–28, 2024. V12CT32A014. ASME. https://doi.org/10.1115/GT2024-123051

LATTICE-BOLTZMANN MODELLING OF INTERNAL COMPRESSIBLE FLOWS: APPLICATION TO THE TRANSONIC LS89 CASCADE

Iason Tsetoglou[1], Song Zhao[1], Jérôme Jacob[1], Pierre Boivin[1,*]

[1]Aix Marseille Univ, CNRS, Centrale Marseille, M2P2, Marseille, France

ABSTRACT

In this work the D3Q19 Hybrid Recursive Regularized Pressure based Lattice Boltzmann Method presented by Farag et al. (2021) is assessed for the simulation of complex transonic internal flows. A Lattice Boltzmann solver presented by Jacob et al. (2018) treating the mass and momentum conservation equations is coupled with a finite volume scheme for the resolution of the conservative form of the total energy equation as shown by Zhao et al. (2020), leading to a fully numerically conservative scheme. The well documented case of the high-pressure turbine guide vane cascade with the VKI LS89 profile is examined. To the authors' knowledge, this is the first numerical aero-thermal investigation of this configuration using a Lattice Boltzmann approach. An appropriate numerical domain along with a grid refinement technique are used to accommodate a Cartesian grid while ensuring flow periodicity downstream of the cascade in the pitch-wise direction. This is verified thanks to the time-averaged profiles of the exit isentropic Mach number and exit isentropic Reynolds number. The solid boundary is introduced in the Cartesian grid with a cut-cell immersed boundary technique where the boundary nodes of the domain are outside of the solid. An efficient treatment for these nodes is used to accurately represent the near wall flow dynamics. An explicit power-law velocity wall model is used to accurately predict the near wall velocities. A logarithmic temperature wall function is also added to this method to improve the convective heat transfer estimation on the blade surface. The results of this study are compared to experimental and numerical results found in literature, proving the LBM to be a viable approach for compressible internal flows.

Keywords: Gas turbine, Internal flow, Turbomachinery, Heat transfer, CFD

NOMENCLATURE

Roman letters

f_i	Population distribution
$\overline{f}_i$	Modified population for 2nd order accuracy
c, τ, ω	Lattice velocity, relaxation time, Gaussian weight
$\mathcal{H}^{(k)}, a^{(n),f}$	Hermite polynomials and moments
ρ, u, p, T	Density, velocity, pressure, temperature
E, e, H, s	Total energy, internal energy, enthalpy, entropy
$\Pi, \mathcal{R}$	Viscous stress tensor, Reynolds stress tensor
q, H_w	Heat flux, wall heat transfer coefficient
k	Wavenumber
F	Force

Greek letters

α, λ	Thermal diffusivity, thermal conductivity
ν, μ	Kinematic viscosity, dynamic viscosity
σ	LB/Finite-difference blending parameter
χ	Spatial wavelength

Dimensionless groups

Re	Reynolds number
Pr	Prandtl number

*Corresponding author: pierre.boivin@univ-amu.fr

M Mach number
θ Non-dimensional temperature
CFL Courant–Friedrichs–Lewy number

Superscripts and subscripts
eq, neq Equilibrium and non-equilibrium
col Post-collision
α, β, γ Space directions
FD, FV Finite-difference, finite-volume
BN Boundary node value
Ref Interpolated value at reference point
$0, 1, 2$ Total, inlet, outlet value
∞, w Free stream and wall value
is Isentropic value
t, sc Turbulent value and shock sensor value
$+, \tau$ Wall unit and friction value

1. INTRODUCTION

The optimal performance of high-pressure turbine vanes in modern gas turbine engines stands as a critical point of interest, driven by the ever-increasing demands for higher Turbine Entry Temperature (TET) and overall pressure ratios (OPR) [1]. These advancements, while promising in enhancing engine efficiency, bring forth formidable challenges. Computational Fluid Dynamics (CFD) has emerged as a powerful tool in understanding the complex flow dynamics and heat transfer phenomena within these turbine components [2]. Among various turbine blade configurations, the LS89 turbine blade cascade has attracted substantial attention due to its sensitivity to turbulence injection and its relevance as a realistic test case, initially studied by Arts et al. in 1990 [3]. Arts et al.'s experimental investigation revolved around a highly loaded transonic turbine nozzle guide vane arranged in a linear cascade configuration. Their comprehensive measurements, conducted in the von Karman Institute's Isentropic Light Piston Compression Tube facility, ensured fidelity in replicating Mach and Reynolds numbers, as observed in modern aero-engines. The experimental program included various measurements, including periodicity checks, blade velocity distribution, convective heat transfer, downstream loss coefficients, exit flow angles, and free-stream turbulence intensity and spectrum measurements [3]. This rigorous exploration involved several combinations of free-stream flow parameters, examining their relative effects on aerodynamic blade performance and convective heat transfer.

The challenges in conducting numerical simulations of such configurations are multiple. Accurately predicting boundary layer transition, heat transfer, and turbulence effects on the LS89 cascade remains a significant hurdle. Current CFD approaches, such as Reynolds-Averaged Navier-Stokes (RANS), Large Eddy Simulation (LES), and Direct Numerical Simulation (DNS), offer differing levels of fidelity and computational costs [2]. Flow prediction is a key element in such problems, and today, Large Eddy Simulation (LES) seems the most promising CFD approach with the potential to provide better insight into the flow dynamics. LES is expected to yield accurate average flow solutions around a blade, showcasing potential for enhanced understanding and predictions. Despite how promising LES is, challenges persist in achieving cost-efficient and accurate simulations with the usual Navier-Stokes solvers, especially in capturing fine-scale turbulence and intricate flow details. This prompts exploration into alternative methods like the Lattice Boltzmann Method (LBM). LBM has emerged as a powerful alternative tool in recent decades. Marié et al. [4] conducted a comparison between LBM and high-order Navier-Stokes schemes for computational aeroacoustics and it was found that the LBM is less dissipative than high order Navier-Stokes schemes and less dispersive than a second order in space with a 3-step Runge-Kutta scheme in time. Its low dissipation properties, together with a simple and easily parallelizable algorithm and an ability to handle complex geometries thanks to immersed boundary conditions on a Cartesian mesh have made it competitive for both academic and industrial applications [4–6].

The VKI LS89 turbine cascade flow has been replicated numerically by a wide variety of CFD methods [7–11]. Though, to the authors' knowledge, no attempt has been made to replicate such a flow problem using a Lattice Boltzmann method. The present work was carried out on the ProLB code, a high-fidelity wall-modelled LES LBM solver aimed for simulating complex industrial flows. Specifically, a D3Q19 Hybrid Recursive Regularized Pressure based Lattice Boltzmann Method (HRR-p LBM) presented by Farag et al. [12] is used. This consists of a Lattice Boltzmann solver presented by Jacob et al. [13] treating the mass and momentum conservation equations, later coupled with a finite volume scheme for the resolution of the non-conservative entropy equation by Guo et al. [14]. Later, an effort was put to restore conservativity [15] for the case of compressible flows, where Wissocq et al. [16] managed to develop a finite-volume scheme, intimately related to the mass and momentum LB fluxes and linearly equivalent to the entropy equation, to solve the total energy equation. The conservative nature of this scheme, and its ability to handle flow discontinuities such as shocks, was demonstrated by the work of Coratger et al. [17] on external transonic flow problems. The aim of the present work is to improve and extend the validity of this method in the case of internal compressible flows. Furthermore, temperature wall-modelling has been added to this method to improve the near wall temperature evaluation in order to expand the capabilities of ProLB for aerothermal studies in complex industrial flows.

This work is organized in the following manner. The hybrid HRR-p Lattice Boltzmann method with total energy conservation is presented in Section 2. In Section 3 the method is applied on different flow configurations of the LS89 cascade and validated against experimental and numerical reference data. Finally, some concluding remarks and perspectives will be discussed in Section 4.

2. LATTICE-BOLTZMANN MODELLING FOR COMPRESSIBLE FLOWS

2.1 Macroscopic governing equations: Navier-Stokes equations

In the HRR-p LBM method [12, 17, 18] a Lattice Boltzmann solver is used for the treatment of the mass and momentum conservation equations:

$$\frac{\partial \rho}{\partial t} + \frac{\partial \rho u_\alpha}{\partial x_\alpha} = 0 \tag{1}$$

$$\frac{\partial \rho u_\alpha}{\partial t} + \frac{\partial \left[\rho u_\alpha u_\beta + \delta_{\alpha\beta} p - \Pi_{\alpha\beta}\right]}{\partial x_\beta} = 0 \tag{2}$$

Alongside them the total energy equation in the conservative form is solved by a finite volume/difference (FV/FD) scheme:

$$\frac{\partial \rho E}{\partial t} + \frac{\partial \rho H u_\alpha}{\partial x_\alpha} = \frac{\partial \Pi_{\alpha\beta} u_\beta}{\partial x_\alpha} - \frac{\partial q_\beta}{\partial x_\beta} \tag{3}$$

where ρ, u_α, p, E are the density, velocity vector, thermodynamic pressure and the total energy of the fluid respectively. The total enthalpy reads $H = E + p/\rho = e + \frac{1}{2}u_\alpha u_\alpha + p/\rho$, with $e = C_v T$ the internal energy for an ideal gas and C_v the specific heat capacity. The viscous stress tensor $\Pi_{\alpha\beta}$ and the heat flux q_β are expressed as:

$$\Pi_{\alpha\beta} = \mu \left(\frac{\partial u_\alpha}{\partial x_\beta} + \frac{\partial u_\beta}{\partial x_\alpha} - \delta_{\alpha\beta} \frac{2}{3} \frac{\partial u_\gamma}{\partial x_\gamma} \right) \tag{4}$$

$$q_\beta = -\lambda \frac{\partial T}{\partial x_\beta} \tag{5}$$

with μ and λ being the dynamic viscosity and thermal conductivity of the fluid. For the closure of the above system, the ideal gas equations of state (EoS) is used:

$$p = \rho r T \tag{6}$$

with $r = R/W$ the specific gas constant, R the universal gas constant and W the molecular weight.

For the hybrid LBM method used in this work, we also introduce a thermodynamic quantity θ defined as:

$$\theta = \frac{T}{T_0} = \frac{rT}{c_s^2} \tag{7}$$

which represents the ratio of the thermodynamic perfect gas pressure to the classical athermal LBM pressure $p = \rho c_s^2$. Attention must be drawn to the fact that c_s is a constant characteristic lattice velocity, $c_s \equiv \Delta x/(\sqrt{3}\Delta t)$, not to be confused with the temperature-dependent physical sound speed defined as $a_s^2 = \gamma r T$.

2.2 Lattice Boltzmann model for mass and momentum conservation

The LB framework is based on the kinetic theory of gases at a mesoscopic scale [6], where the fluid is represented in a discrete manner through the particle distribution function $f_i(\mathbf{x}, \mathbf{c}_i, t)$, depending on the position $\mathbf{x}$, a finite discrete set of Q particle velocities $\mathbf{c}_i$ and time t, with $i \in [0, Q-1]$. This pressure based method relies on a D3Q19 lattice with a distribution function f_i defined such that the moments of the equilibrium distribution function f_i^{eq} satisfy the following relations:

$$\sum_i f_i^{\mathrm{eq}} = \rho \tag{8}$$

$$\sum_i c_{i\alpha} f_i^{\mathrm{eq}} = \rho u_\alpha \tag{9}$$

$$\sum_i c_{i\alpha} c_{i\beta} f_i^{\mathrm{eq}} = \rho u_\alpha u_\beta + \rho \theta c_s^2 \delta_{\alpha\beta} \tag{10}$$

which obeys a classical single relaxation time evolution, based on the Bhatnagar-Gross-Krook (BGK) model [19], through the Lattice Boltzmann Equation (LBE) with a stream-collide splitting between advection and collision steps. In the absence of external forces the LBE reads:

$$\frac{\partial f_i}{\partial t} + c_{i\alpha} \frac{\partial f_i}{\partial x_\alpha} = -\frac{1}{\tau}(f_i - f_i^{\mathrm{eq},19r}) + F_i \tag{11}$$

where $\tau = \mu/(\rho c_s^2)$ is the relaxation time toward equilibrium and F_i an arbitrary force.

Before the collision procedure, the macroscopic variables $\rho(t+\Delta t, \mathbf{x})$ and $(\rho u_\alpha)(t+\Delta t, \mathbf{x})$ need to be updated based on the post-streaming populations f_i of the previous time-step. In parallel, the scalar energy equation is advanced by a FV scheme as shown in Section 2.3, allowing us to compute the energy at the next time step as well as the temperature:

$$T = (E - \frac{1}{2} u_\alpha u_\alpha)/C_v \tag{12}$$

A Crank–Nicolson like scheme is used to discretize the LBE in space and time [6]. To remove the implicit treatment of the equation and retain second-order accuracy in time, a new distribution and relaxation time are defined as:

$$\overline{f}_i = f_i - \frac{\Delta t}{2\tau}(f_i^{\mathrm{eq}} - f_i) - \frac{\Delta t}{2} F_i \tag{13}$$

$$\overline{\tau} = \tau + \Delta t/2 \tag{14}$$

The post-collision distribution $\overline{f}_i^{\mathrm{col}}$ at time-step $t + \Delta t$ is evaluated as:

$$\overline{f}_i^{\mathrm{col}} = f_i^{\mathrm{eq}} + \left(1 - \frac{\Delta t}{\overline{\tau}}\right) \overline{f}_i^{\mathrm{neq}} + \frac{\Delta t}{2} F_i^c \tag{15}$$

Equation 15 brings the populations f_i back to a modified pressure based equilibrium distribution f_i^{eq} evaluated from its projection onto the D3Q19 rotational symmetry basis of Gauss-Hermite polynomials up to third order:

$$\begin{aligned} f_i^{\mathrm{eq}} = \omega_i \Bigg[& \rho + \frac{\omega_i - \delta_{0i}}{\omega_i} \rho(\theta - 1) + \frac{\mathcal{H}_{i\alpha}^{(1)}}{c_s^2} \rho u_\alpha \\ & + \frac{\mathcal{H}_{i\alpha\beta}^{(2)}}{2c_s^4} \rho u_\alpha u_\beta + \frac{\mathcal{H}_{i\gamma}^{(3r)}}{6c_s^6} \rho u_\alpha u_\beta u_\gamma \Bigg] \end{aligned} \tag{16}$$

where ω_i is the Gaussian weight associated with the discrete velocity $\mathbf{c}_i$. The unusual Kronecker δ_{0i} serves to make this model equivalent to the classical density-based LB model with additional information projected onto fourth order polynomials [18]. A hybrid recursive regularized collision (HRR) kernel [13] is implemented to recover a correct viscous stress tensor. A regularized distribution function is introduced prior to the collision step through recomputing the off-equilibrium distribution $\overline{f}_i^{\mathrm{neq}}$ for the viscous tensor are evaluated as:

$$\overline{f}_i^{\mathrm{neq}} = \omega_i \left[\frac{\mathcal{H}_{i\alpha\beta}^{(2)}}{2c_s^4} \tilde{a}_{\alpha\beta}^{(2),\,\mathrm{neq}} + \frac{\mathcal{H}_{i\alpha\beta\gamma}^{(3r)}}{6c_s^6} a_{\alpha\beta\gamma}^{(3r),\,\mathrm{neq}} \right] \tag{17}$$

where the third order off-equilibrium $a_{\alpha\beta\gamma}^{(3r),\,\mathrm{neq}}$ is recursively derived. Further details about the collision operation and the Gauss-Hermite polynomials are presented in Appendix A of Ref. [18]. The forcing term F_i^c is needed to enforce conservativity by balancing the errors induced by the truncation of the polynomial expansion of the Maxweillian and the quadrature error associated with the lattice [12, 15, 20, 21]. Its evaluation is based on the formulation presented in Ref. [18].

In the HRR kernel the off-equilibrium stress tensor $\tilde{a}_{\alpha\beta}^{(2),\,\mathrm{neq}}$ is computed as a combination of two contributions. The first is evaluated by the direct projection of the non-equilibium distribution function:

$$\overline{a}_{\alpha\beta}^{(2),\,\mathrm{neq,\,PR}} = \mathcal{H}_{i\alpha\beta}^{(2)} \overline{f}_i^{\mathrm{neq}} \tag{18}$$

The second is the evaluated Navier-Stokes viscous stress tensor by a FD scheme (2nd order in the core of the fluid and decentered 1st order at the boundary nodes):

$$\overline{a}_{\alpha\beta}^{(2),\,\mathrm{neq,\,FD}} = -\rho c_s^2 \overline{\tau} \left(\frac{\partial u_\alpha}{\partial x_\beta} + \frac{\partial u_\beta}{\partial x_\alpha} - \delta_{\alpha\beta} \frac{2}{3} \frac{\partial u_\gamma}{\partial x_\gamma} \right) \tag{19}$$

The final stress tensor can then be expressed as a blending of these two contributions:

$$\begin{aligned} \tilde{a}_{\alpha\beta}^{(2),\,\mathrm{neq}} = \sigma & \left[\overline{a}_{\alpha\beta}^{(2),\,\mathrm{neq,\,PR}} - \frac{\delta_{\alpha\beta}}{3} \overline{a}_{\gamma\gamma}^{(2),\,\mathrm{neq,\,PR}} \right] \\ & + (1 - \sigma)\, \overline{a}_{\alpha\beta}^{(2),\,\mathrm{neq,\,FD}} \end{aligned} \tag{20}$$

with $\sigma \in [0, 1]$ a free parameter. Using the traceless Lattice Boltzmann stress tensor improves the numerical stability by filtering an additional non-hydrodynamic mode [13, 16].

Finally, streaming the collision population f_i^{col} at time-step t to the neighbor lattice points we obtain the following post-streaming population:

$$\overline{f}_i(t + \Delta t, \mathbf{x}) = \overline{f}_i^{\mathrm{col}}(t, \mathbf{x} - \mathbf{c}_i \Delta t) \tag{21}$$

which constitutes the base for the next time-step calculations, closing a collision-streaming iteration.

2.3 Finite Volume scheme for energy conservation

The present method is based on a hybrid segregated method where the temperature fluctuations are not considered in the LB solver, but solved by a separate finite-volume form of the energy equation. Usually the non-conservative advection equation of the entropy is used as it is a characteristic variable of the Euler system

$$\frac{\partial s}{\partial t} + u_\alpha \frac{\partial s}{\partial x_\alpha} = 0 \tag{22}$$

which after a linearity assumption is completely decoupled from the isothermal LB scheme for mass and momentum. But this formulation is not conservative, hence not a suitable choice for handling discontinuities [15].

To remedy that while keeping the advantages of the entropy equation, a total energy equation has been proposed by Ref. [16] based on a linear equivalence with Eq. 22. The LB scheme is also expressed under a FV form involving fluxes, which are introduced in the total energy equation as numerical corrections. The left hand side (LHS) of Eq. 3 can be expressed as:

$$\frac{\delta(\rho E)}{\delta t} + \frac{\delta F^{\rho E}_{\mathbf{x}+\Delta x_\alpha/2}}{\delta x_\alpha} = 0 \tag{23}$$

where δ is an operator denoting a discrete scheme. The term $F^{\phi}_{\mathbf{x}+\Delta x_\alpha/2}$ represents the inter-cell flux of a variable ϕ in a FV scheme between the cells with centers at positions $\mathbf{x}$ and $\mathbf{x}+\Delta\mathbf{x}$. The total energy flux reads:

$$\begin{aligned} F^{\rho E}_{\mathbf{x}+\Delta x_\alpha/2} = & \underbrace{\mathcal{F}_{\mathbf{x}+\Delta x_\alpha/2}(\rho H u_\alpha)}_{\text{Total energy flux}} \\ & + \underbrace{(h-\kappa)\left[F^{\rho}_{\mathbf{x}+\Delta x_\alpha/2} - \mathcal{F}_{\mathbf{x}+\Delta x_\alpha/2}(\rho u_\alpha)\right]}_{\mathscr{M}} \\ & + \underbrace{u_\beta\left[F^{\rho u_\beta}_{\mathbf{x}+\Delta x_\alpha/2} - \mathcal{F}_{\mathbf{x}+\Delta x_\alpha/2}(\rho u_\alpha u_\beta + p\delta_{\alpha\beta})\right]}_{\mathscr{P}} \end{aligned} \tag{24}$$

The fluxes $F^{\rho}_{\mathbf{x}+\Delta x_\alpha/2}$ and $F^{\rho u_\beta}_{\mathbf{x}+\Delta x_\alpha/2}$ along the 3 Cartesian directions are directly computed from the LB scheme fluxes over the Q discrete lattice directions. The interested reader can read Ref. [16] for the exact relationship on the D3Q19 lattice used. The fluxes $\mathcal{F}_{\mathbf{x}+\Delta x_\alpha/2}(\psi)$ represent a linear function of the scalar field ψ in such a way that $\mathcal{F}_{\mathbf{x}+\Delta x_\alpha/2}(\psi) = \psi + O(\Delta x)$. This function depends on the entropy scheme that one wants to mimic, in particular its spatial derivative. In this work the MUSCL-Hancock scheme has been adopted, as presented in Appendix C of Ref. [17]. Taking a look at the RHS terms of Eq. 24, the first is simply the total energy flux $\rho H u_\alpha$ discretized by the linear scheme $\mathcal{F}_{\mathbf{x}+\Delta x_\alpha/2}$. The term $\mathscr{M}$ serves to restore the consistency between the total energy scheme and the mass conservation discretized by a different scheme (LB scheme). The third terms restores consistency between the total energy scheme and the discrete momentum equation. It is also shown that in the low-Knudsen limit $\mathscr{P} \approx -u_\beta \Pi_{\alpha\beta} + O(\Delta x)$. This term contributes for the viscous heat effects appearing in the Navier-Stokes equation. Wissocq et al. [16] argued that thanks to this implicit contribution, the viscous heat term in the RHS of Eq. 3 does not need to be explicitly computed. Finally, to extend this energy scheme to viscous flows, one simply needs to replace the "Euler" flux in Eq. 23 by the Navier-Stokes flux by discretizing the conduction term of Eq. 3:

$$F^{\rho E,\mathrm{NS}}_{\mathbf{x}+\Delta x_\alpha/2} = F^{\rho E}_{\mathbf{x}+\Delta x_\alpha/2} - \lambda \frac{\delta\, T_{\mathbf{x}+\Delta x_\alpha}}{\delta x_\alpha} \tag{25}$$

2.4 Sub-grid turbulence model

In the Large-Eddy Simulation (LES) approach, part of the turbulent spectrum, i.e. the larger eddies, are resolved while the smallest vortical structures are modelled. Essentially, the scale separation is achieved by applying a low-pass filter for the turbulence. In the momentum filtered equation the sub-grid scale Reynolds stress tensor $\mathcal{R}_{\alpha\beta} = \overline{\rho}(\widetilde{u_\alpha u_\beta} - \tilde{u}_\alpha \tilde{u}_\beta)$ appears, which is unresolved and needs to be modeled. In this work, the model proposed by Vreman in Ref. [22] is used based on the Boussinesq approximation, where:

$$\mathcal{R}_{\alpha\beta} - \frac{1}{3}\mathcal{R}_{\gamma\gamma}\delta_{\alpha\beta} = -2\mu_t\left(\widetilde{S}_{\alpha\beta} - \frac{1}{3}\widetilde{S}_{\gamma\gamma}\delta_{\alpha\beta}\right) \tag{26}$$

with $\widetilde{S}_{\alpha\beta} = \frac{1}{2}\left(\frac{\partial \tilde{u}_\alpha}{\partial x_\beta} + \frac{\partial \tilde{u}_\beta}{\partial x_\alpha}\right)$. The sub-grid scale eddy viscosity is modeled as:

$$\mu_t = 2.5\,\overline{\rho} C_s^2 \sqrt{\frac{B_\beta}{\alpha_{ij}\alpha_{ij}}} \tag{27}$$

where:

$$\alpha_{ij} = \frac{\partial \tilde{u}_j}{\partial x_i}, \quad \beta_{ij} = \Delta_m^2 \alpha_{mi} \alpha_{mj}$$
$$B_\beta = \beta_{11}\beta_{22} - \beta_{12}^2 + \beta_{11}\beta_{33} - \beta_{13}^2 + \beta_{22}\beta_{33} - \beta_{23}^2 \tag{28}$$

and C_s is the Smagorinsky constant [23]. This model has been shown to be more accurate than the Smagorinsky model and as good as the standard dynamic model of Germano et al. [24] for transitional and turbulent flows. Effectively, in LBM this is equivalent to modifying the relaxation time by taking into account the added eddy viscosity:

$$\overline{\tau} = \frac{\Delta t}{2} + \frac{\mu + \mu_t}{\rho c_s^2} \tag{29}$$

A sub-grid scale thermal conductivity has also been defined as:

$$\lambda_t = \mu_t c_p / \mathrm{Pr}_t \tag{30}$$

2.5 Shock capturing

Shock capturing techniques aim to automatically mitigate the Gibbs phenomenon [25], reducing the oscillations created near discontinuities. These methods leverage the effects of dissipative mechanisms on shocks [26], employing artificial dissipation via an added numerical viscosity in the conservation equations to enhance shock thickness, making it comparable to the local mesh size. To detect shocks accurately, a shock sensor based on the Jameson-Schmidt-Turkel (JST) scheme [27] is employed:

$$\nu_{sc} = \left| \frac{\rho_{i-1} - 2\rho_i + \rho_{i+1}}{\rho_{i-1} + 2\rho_i + \rho_{i+1}} \right| \tag{31}$$

After summation over all space dimensions this term is multiplied by a free parameter s_{sc} and added as an artificial viscosity to the relaxation time:

$$\overline{\tau} = \frac{\Delta t}{2} + \frac{\mu + \mu_t + \rho \nu_{sc} s_{sc}}{\rho c_s^2} \tag{32}$$

2.6 Explicit power-law velocity wall model in LBM

The wall model used in this work is based on the one-seventh power-law introduced by Prandtl. The exponent of $1/7$ has been used recently by various authors for LES [28–30]. The equilibrium power-law model used is defined as in Ref. [30] and Ref. [31].

$$u^+ = \begin{cases} y^+ & \text{if } y^+ \leq y_c^+ \\ A\,(y^+)^B & \text{if } y^+ \geq y_c^+ \end{cases} \tag{33}$$

with $B = 1/7$. $y^+ = 11.81$ is the scaled height of the viscous sub-layer [32]. By the continuity of the velocity profile at y_c^+ we can deduce that $A = (y_c^+)^{1-B} \approx 8.3$. Taking into consideration the following relations:

$$u^+ = \frac{u_t}{u_\tau} \quad \text{and} \quad y^+ = \frac{y u_\tau}{\nu} \tag{34}$$

where u_t is only the tangential velocity component, we can obtain an explicit formula for the friction velocity u_τ at a distance y from the wall (in non scaled units):

$$\frac{u_t}{u_\tau} = A \left(\frac{y u_\tau}{\nu} \right)^B \tag{35}$$

leading to the explicit relation:

$$u_\tau = u_t^{\frac{1}{1+B}} A^{\frac{-1}{1+B}} y^{\frac{-B}{1+B}} \nu^{\frac{B}{1+B}} \tag{36}$$

At this point, it should be reminded that in this LBM approach we use a cut-cell immersed boundary method with a Cartesian grid whose points are defined only in the fluid domain. For such configurations, Ref. [33] proposes to use a model to mimic a body-fitted grid. In order to reconstruct the velocity at the boundary nodes based on a wall model, we need to define a fictitious point on the wall normal line that passing through the boundary node at an arbitrary distance from the wall surface as shown in Fig. 1. This point is placed $2.5\Delta x$ from the wall, Δx being the local mesh size near the wall. All quantities found on this point are followed by the subscript *Ref* and are computed by an Inverse Distance Weighting (IDW) interpolation from the surrounding fluid nodes. The previous combination of linear and power-law models is used on the fictitious reference point *Ref*:

$$u_{Ref}^+ = \begin{cases} y_{Ref}^+ & \text{if } y_{Ref}^+ \leq y_c^+ \\ A \left(y_{Ref}^+ \right)^B & \text{if } y_{Ref}^+ \geq y_c^+ \end{cases} \tag{37}$$

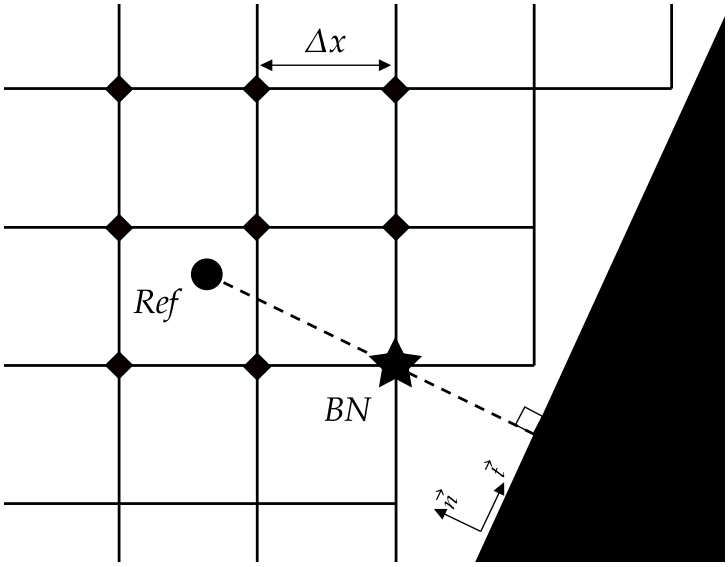

FIGURE 1: NEAR-WALL TREATMENT SCHEME IN LBM. ⋆: BOUNDARY NODE, • : REFERENCE POINT AT A DISTANCE OF 2.5Δx FROM THE WALL, ♦: CONTRIBUTING NODES FOR INTERPOLATION

If $y^+_{Ref} \leq y^+_c$, it implies that both the reference point and the boundary node are within the viscous sub-layer, hence:

$$\frac{u_{t,BN}}{u_{t,Ref}} = \frac{y_{BN}}{y_{Ref}} \Leftrightarrow u_{t,BN} = u_{t,Ref}\frac{y_{BN}}{y_{Ref}} \tag{38}$$

If $y^+_{Ref} \geq y^+_c$, we can assume that the boundary node is also in the power-law region.

$$\frac{u_{t,BN}}{u_{t,Ref}} = \left(\frac{y_{BN}}{y_{Ref}}\right)^B \Leftrightarrow u_{t,BN} = u_{t,Ref}\left(\frac{y_{BN}}{y_{Ref}}\right)^B \tag{39}$$

Effectively, by dividing the expression of u^+ at the boundary node, from Eq. 33, by its expression at the reference point, from Eq. 37, we manage to obtain directly the non-scaled tangential velocity at the boundary node $u_{t,BN}$ without the need to compute the friction velocity u_τ at all. This solution offers a very simple to implement wall model for Cartesian grids.

2.7 Thermal wall law

The thermal wall law adopted in this work is based on the Kader temperature wall function found in Ref. [34, 35], which represents a unified model for both the linear profile in the viscous sub-layer and the logarithmic profile in the inertial zone. This addition serves to better predict the temperature on the boundary nodes, along with the wall heat transfer, without having to fully resolve the turbulent thermal boundary layer.

The non-dimensional temperature is first evaluated at the *Ref* point:

$$\begin{aligned} T^+_{Ref} = &\,\mathrm{Pr}\, y^+_{Ref}\exp\left(-\Gamma\right) \\ &+ \left[\frac{\mathrm{Pr}_t}{0.4}\ln(1+y^+_{Ref}) + \beta_T\right]\exp\left(-1/\Gamma\right) \end{aligned} \tag{40}$$

where $\Gamma = \frac{0.01(\mathrm{Pr}y^+)^4}{1+5\mathrm{Pr}^3 y^+}$, $\beta_T = (3.85\mathrm{Pr}^{1/3} - 1.3)^2 + 2.12\ln(\mathrm{Pr})$ and $\mathrm{Pr}_t = 0.85$.

Then the friction temperature T_τ is evaluated as:

$$T_\tau = (T_w - T_{Ref})/T^+_{Ref} \tag{41}$$

The non-dimensional temperature at the boundary node T^+_{BN} can be computed based on y^+_{BN} through Eq. 40 and finally the temperature at the boundary node is estimated as:

$$T_{BN} = T_w - T_\tau T^+_{BN} \tag{42}$$

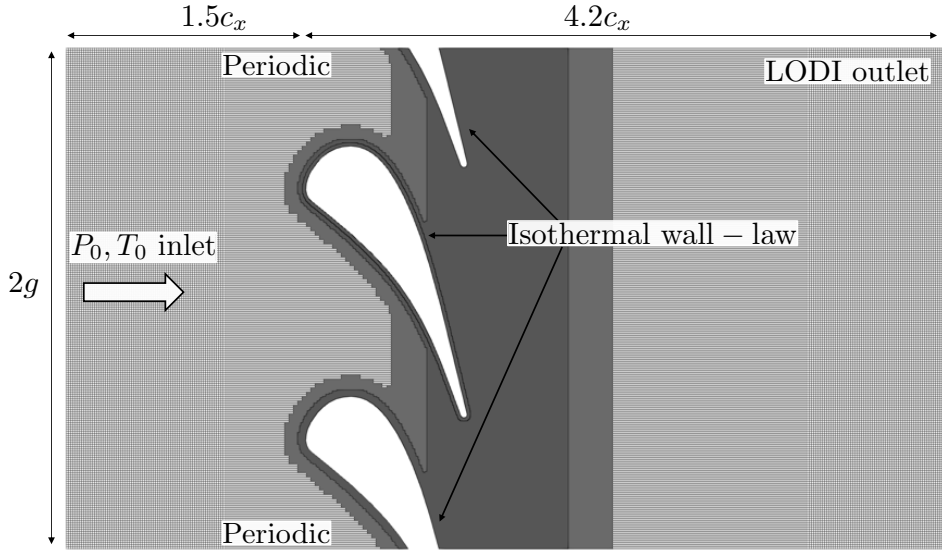

FIGURE 2: COMPUTATIONAL DOMAIN AND BOUNDARY CONDITIONS

TABLE 1: FLOW CONFIGURATIONS

Case	P_0 [bar]	T_0 [K]	T_w [K]	$M_{2,is}$	$Re_{2,is}$
MUR129	1.849	409.2	297.75	0.84	1.13×10^6
MUR44	1.433	421.8	300.00	0.84	1.00×10^6
MUR47	1.596	418.0	300.00	1.02	1.00×10^6

3. APPLICATION ON THE LS89 CASCADE

3.1 Numerical set-up

The HRR-p model described in the previous section is applied to the internal compressible flow of the VKI LS89 turbine blade cascade. The usual way to generate the computational domain is to simulate one blade and expand the domain of half a pitch length ($g/2$) in both directions along the blade chord c, so that the domain follows the streamlines of the flow. In LBM, however, it is hard to implement periodic boundary conditions (BC) on curved boundaries due to the Cartesian mesh. Thus a rectangular domain is used with periodic top and bottom boundaries. The height of the domain is equal to two pitch lengths ($2g$). The domain is shown in Fig. 2 specifying its dimensions and the BC surfaces. The blade chord is $c = 67.647$mm, its projection on the horizontal axis is $c_x = 36.461$mm and the pitch is $g = 0.85c$. The inlet BC imposes the total pressure P_0, total temperature T_0 and direction of the incoming flow [36, 37] while at the outlet the far-field static pressure is imposed along with a viscous sponge layer, which modifies directly the value of $\overline{\tau}$ in Eq. 15, to allow the outgoing waves to leave the domain while dampening any reflections. Finally at the blade walls, wall-modelling is used for the velocity (Section 2.6) and the temperature (Section 2.7).

The domains used include $N = \{1, 2, 3\}$ refinement levels near the blades and their wakes where the local grid spacing is equal to $\Delta x_N = \Delta y_N = \Delta z_N = 5 \times 10^{-4}/2^N$ m. The span of the domain is equal to Δz_0, effectively rendering the simulation to a 2-dimensional flow. In literature, the usual approach of simulating this configuration is with wall-resolved meshes (either RANS or LES [8, 9]), i.e. with $\Delta y^+ \approx 1$. This can be computationally expensive resulting in a large number of computational elements in the mesh. On the contrary, the present work was carried out on the ProLB code, a high-fidelity wall-modelled LES solver aimed for predicting industrial flow problems around complex geometries. The main objective is to achieve accurate predictions on the dynamics of the fluid, while maintaining competitive turnaround times. Thus, the use of a larger grid spacing along with the use of near-wall modelling is favoured in this study. The average y^+ value measured at the boundary nodes along the blade surface s for the 3 refinement levels are 71, 40 and 22 respectively. The curvilinear abscissa s represents the blade surface, where $s = 0$ is the leading edge (LE), $s = [-60, 0]$ is the pressure side from the trailing edge (TE) to the LE and $s = [0, 80]$ is the suction side from the LE to the TE. The local time step is calculated based on a CFL of 0.15 as $\Delta t_N = \text{CFL} \times \Delta x_N / |u_\infty + \sqrt{\gamma r T_\infty}|$, since values higher than 0.2 cause stability issues. The LB/FD blending parameter for the off-equilibrium populations is set to $\sigma = 0.95$. The simulations initially ran for 30 convective flow-through periods $T_c = c/U_\infty$, based on the upstream velocity $U_\infty = 60.7$ m/s and the blade chord length c, until a converged state was reached and statistics were gathered over 15 additional periods. The cases examined in this work had a free-stream turbulence intensity of $Tu \leq 1\%$ in the experiments of Arts. In numerical simulations such a low value barely influences the flow profile and can be safely omitted by setting $Tu = 0\%$. The specific

TABLE 2: MUR129 COMPUTATIONAL SET-UP, CPU HOURS PER CHORD FLOW-THROUGH PERIOD AND REDUCED COMPUTATIONAL TIME FOR DIFFERENT GRID RESOLUTIONS

N	$c/\Delta x_N$	N_{nodes}	N_{CPU}	hCPU/T_c	RCT [μs]
1	270	2.58×10^5	32	4.29	4.26
2	540	1.14×10^6	48	42.1	4.73
3	1080	1.40×10^6	80	65.7	3.01

TABLE 3: MUR129 EXIT FLOW CONDITION ERRORS FOR DIFFERENT GRID RESOLUTIONS

N	$M_{2,is}$	$Re_{2,is}$	$\varepsilon(M_{2,is})$	$\varepsilon(Re_{2,is})$
1	0.839	1.137×10^6	0.062 %	0.116 %
2	0.840	1.138×10^6	0.037 %	0.258 %
3	0.842	1.140×10^6	0.233 %	0.380 %

flow configurations for the cases examined in this work can be found in Table 1.

3.2 Aerodynamic study

A grid-convergence study was carried out for the MUR129 case on three grid resolutions ($N = \{1, 2, 3\}$), where the mean aerodynamic quantities of interest where examined. Table 2 lists the near wall grid spacing, the total number of grid points, the number of CPU processors used, the CPU hour cost per convective flow-through period and the reduced computational cost in $\mu\text{s}/\text{N}_{\text{iter}}/\text{N}_{\text{nodes}}$ for each grid resolution.

First, we need to verify that the exit flow conditions match well with the experimental ones. The downstream static pressure P_2 measurements are taken on a plane parallel to the TE, at $x = 1.4c_x$. Then, the isentropic Mach number can be computed based on the upstream total pressure P_0, as:

$$M_{is} = \sqrt{\frac{2}{\gamma - 1}\left(\left(\frac{P_0}{P}\right)^{\frac{\gamma-1}{\gamma}} - 1\right)} \tag{43}$$

where P is the static pressure, along with the local Reynolds number $Re_{is} = a_s M_{is} c/\nu$. Table 3 demonstrates that for all grid resolutions both the $M_{2,is}$ error and the $Re_{2,is}$ error remain less than 1% compared to the experimental values reported in Ref. [3]. Figure 3 shows their evolution along the pitch direction for $N = 1$, which also serves to verify the periodicity of the flow.

The isentropic Mach number evolution along the surface of the blade is also plotted in Fig. 4 for the grid resolutions of $N = 1$ and $N = 3$, compared to wall resolved LES results from the study in Ref. [10]. It should be noted that the simulation results are almost identical for both grid resolutions. Further examining the results, the stagnation point is well placed at $s = 0$ mm where $P_0/P = 1$. On the suction side, from the LE up to $s = 20$ mm the flow steeply accelerates along the surface. Then, up to $s = 30$ mm a slight plateau is observed. A slight re-acceleration after $s = 30$ mm is reported followed by a rather flat evolution of the velocity distribution due to the presence of a weak adverse pressure gradient (APG) starting after $s = 40$ mm. The HRR-p method predicts the second acceleration and the evolution of M_{is} approaching the TE. The APG, which we manage to predict, is sufficiently weak so that no specific correction is needed to the velocity wall model. Along the pressure side, the velocity distribution varies smoothly, with no existence of a velocity peak downstream of the leading edge, matching perfectly with the reference numerical values. This also corresponds well to the experimental observations of Arts et al. [3] where, for the cases of low-intensity free-stream turbulence, the boundary layer remains in a laminar state.

At this point, the authors would like to address the oscillations observed in Fig. 4 caused by pressure oscillations at the wall in the region of $s = [15, 40]$ mm. These are non-physical artifacts from the LB solver linked to the stair-case effect due to the Cartesian grid around curved boundaries. A frequency analysis (not shown in this work) points at a direct link between the wave number $k = 2\pi/\chi$, where χ is the wavelength of the oscillations, and the grid spacing Δx_0 such that $k\Delta x_0 = 2^N$. For each grid resolution there are N dominant wave numbers, with corresponding wavelengths $\chi_j = 2\pi\Delta x_0/2^j$, $j \in [1, ..., N]$.

Having validated that $N = 1$ is sufficient for the estimation of mean aerodynamic quantities, this resolution was used to predict the flow of the subsonic MUR44 and transonic MUR47 cases. According to the experimental observations of Arts et al. [3], the evolution of the isentropic Mach number along the blade for the MUR44 configuration is almost identical to that of MUR129. In this case we observe again a very good agreement between the predicted values and the experimental data. In the MUR47 configuration, the isentropic Mach number evolution is similar to that of the MUR129 case, except for the fact that instead of plateauing after $s = 40$ mm, the fluid accelerates further leading to a shock formation around $s = [65, 75]$ mm. Figure 5 shows that for $s = [-60, 35]$ mm, the M_{is} is predicted perfectly. Similar to MUR129, our method suffers from some non-physical oscillations around $s = [20, 45]$ mm. The large peak around $s = 35$ mm seems to be influenced by the high velocities at the trailing edge of the upper blade of the cascade, as it can be seen in Fig. 6. With higher grid resolution this peak should become less pronounced. After $s = 40$ mm the fluid successfully accelerates to $M_{is} > 1$, despite the

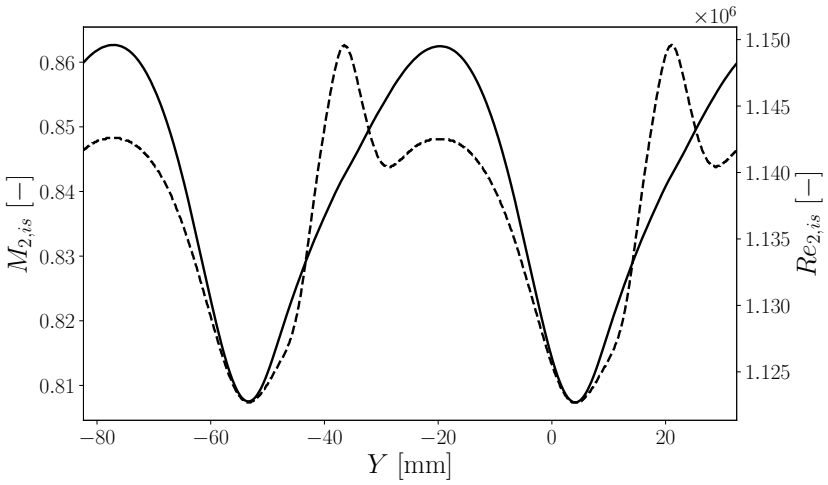

FIGURE 3: MUR129 EXIT ISENTROPIC MACH AND REYNOLDS NUMBERS WITH N=1. −: $M_{2,is}$, −−: $Re_{2,is}$

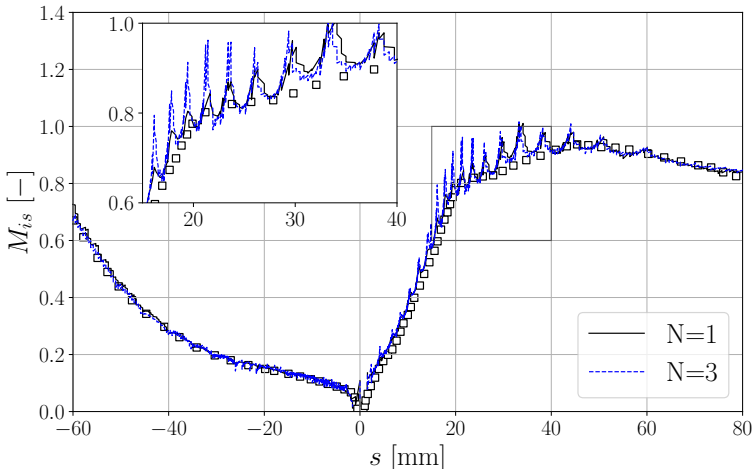

FIGURE 4: MUR129 ISENTROPIC MACH NUMBER DISTRIBUTION ON THE BLADE FOR DIFFERENT REFINEMENT LEVELS. □: WRLES RESULTS [8], −: HRR-*p* N=1, −−: HRR-*p* N=3

small oscillations, and finally the shock position is well-predicted near $s = 70$ mm. These observations can be further supported by the mean numerical Schlieren field, $\ln(1+ \mid \nabla\rho \mid)$, in Fig. 6, where the iso-value contour of $M_{is} = 1$ is also plotted.

3.3 Heat transfer study

In the current work, the near-wall heat transfer q_w is calculated between the wall and a fictitious point, defined in the same way as the *Ref* point, at a distance of Δx from the wall as follows:

$$q_w = -\rho c_p(\alpha + \alpha_t)\frac{(T_{\Delta x} - T_w)}{\Delta x} \tag{44}$$

where $\alpha = \nu/\mathrm{Pr}$ and $\alpha_t = \nu_t/\mathrm{Pr}_t$ are the molecular and turbulent thermal diffusivity respectively, with a constant Prandtl number for air equal to 0.7, and 0.85 for the turbulent Prandtl number. The predicted results are compared to the reference data through the wall heat transfer coefficient:

$$H_w = \frac{q_w}{(T_w - T_0)} \tag{45}$$

Figure 7 shows the evolution of H_w along the blade surface of the MUR129 case, compared the experimental measurements of Arts et al. [3].

It can be seen that at the pressure side, the predicted heat transfer coefficient agrees with the experimental values. This is the case due to the relatively well resolved thin laminar boundary layer developed, where a linear behaviour of the flow quantities can be

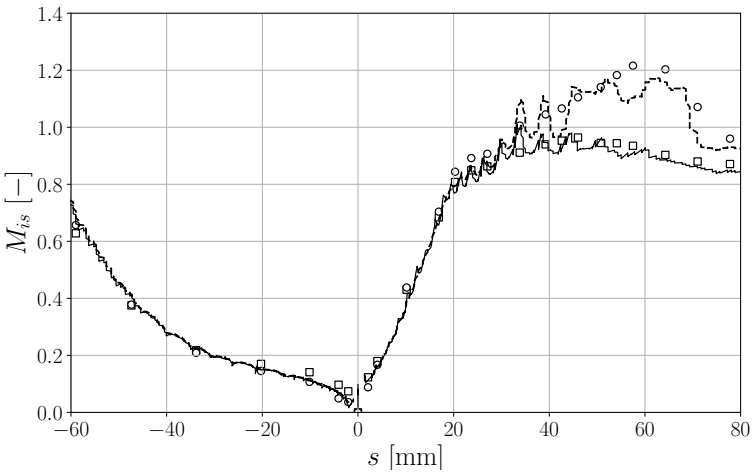

FIGURE 5: ISENTROPIC MACH NUMBER DISTRIBUTION ON THE BLADE. □: MUR44 EXPERIMENTAL RESULTS [3], ∘: MUR47 EXPERIMENTAL RESULTS [3], –: MUR44 HRR-p, ––: MUR47 HRR-p

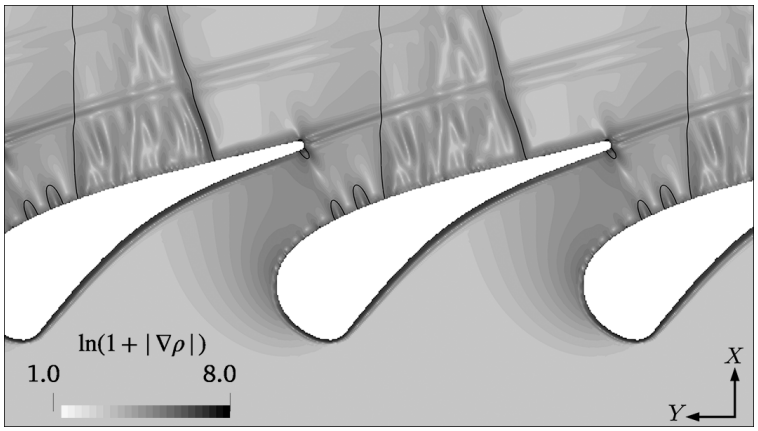

FIGURE 6: MUR47 NUMERICAL SCHLIEREN FIELD

observed. On the suction side the flow is a lot more complex with the existence of a much thicker turbulent boundary layer, where highly non-linear effects dominate the flow and viscous heating is non-negligible. The thermal wall law used manages to predict relatively well the stagnation point and even the initial region of the suction side ($s = [0, 30]$ mm) where the boundary curvature is significant. Although, the heat transfer coefficient also suffers from strong non-physical oscillations in the region of $s = [15, 40]$ mm. In the region of the adverse pressure gradient ($s > 40$ mm) the temperature model falls short in predicting H_w. The exact source of error is not clear yet. It is observed that the turbulent thermal boundary layer was much thicker than expected, and the temperature at the first few near-wall nodes is very close to the wall temperature T_w. It is possible that a more elaborate model for the turbulent diffusivity, compared to Eq. 30, is needed to accurately represent the turbulent mixing contribution $-\widetilde{v'T'}$.

4. CONCLUSION

The aim of this work was to implement a hybrid recursive regularized pressure based (HRR-p) Lattice Boltzmann method, coupled with velocity and temperature wall models, to the compressible internal flow of the LS89 turbine vane cascade. LBM has proven an attractive alternative to usual simulation methods, but has yet to be applied on this type of flow problems. First, the 2D MUR129 case is examined with multiple grid resolution levels, where the mean exit flow conditions are very well predicted compared to experimental values, even for the coarser grid with $c/\Delta x = 270$. On the blade, the mean isentropic Mach number is also very well predicted. Similar results were found for the MUR44 case. In the transonic MUR47 case the method was able to predict very well the position of the shock on a very coarse grid. In all of these studies, less than 1.5×10^6 computational nodes where necessary in the mesh thanks to the use of wall-modelling, which is very promising for the extension of this study to a 3D configuration. A heat transfer study is also conducted on the MUR129 case, where the coupling of a thermal wall model with the HRR-p method is tested. The heat transfer coefficient is predicted very well on the blade, except for the turbulent region on the suction side with the adverse pressure gradient, where the heat

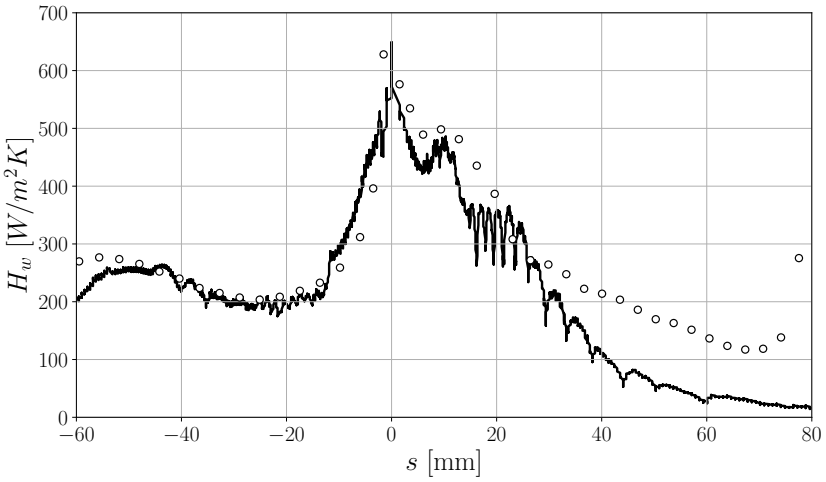

FIGURE 7: MUR129 HEAT TRANSFER COEFFICIENT DISTRIBUTION ON THE BLADE. ∘: EXPERIMENTAL RESULTS [3], –: HRR-p N3

transfer is under-predicted. Although, the cause of this underestimation is not clear yet.

The main axes of improvement were made clear during this work and are in active development:

- Reduction of the non-physical oscillations of the pressure near the suction-side wall.
- Further investigation and validation of the turbulent diffusivity model in order to improve the heat transfer estimation at the turbulent zone of $s > 35$ mm.

Future work will focus on improving the near-wall predictions, as well as applying the Wall-Modelled HRR-p LB method to a wide variety of complex transonic flow configurations.

ACKNOWLEDGMENTS

Part of this research was supported by ANR, Airbus, Fives-Pillard and SafranTech by the Industrial Chair Program Liberty ANR-23-CHIN-0005; and the French project BALBUZARD funded by DGAC and supported by Next generation EU in the frame of "Plan national de Relance et de Résilience français (PNRR)". This project was provided with computer and storage resources by GENCI at TGCC thanks to the grant 2023-A0152A07679 on the supercomputer Joliot Curie SKL/ROME partition. Centre de Calcul Intensif d'Aix-Marseille is acknowledged for granting access to its high performance computing resources. The authors would also like to acknowledge Thibaut Rossi for the fruitful discussions.

REFERENCES

[1] Gorla, Rama S. R. and Khan, Aijaz A. *Turbomachinery: Design And Theory*. No. 160 in *Mechanical engineering*, Marcel Dekker (2003).

[2] Wilcox, David. *Turbulence Modeling For CFD*, 3rd ed. DCW Industries, Incorporated (2006).

[3] Arts, T, de Rouvroit, M Lambert and Rutherford, A.W. "Aero-Thermal Investigation Of A Highly Loaded Transonic Linear Turbine Guide Vane Cascade." Technical Report No. 174. von Karman Institute for Fluid Dynamics. 1990.

[4] Marié, Simon, Ricot, Denis and Sagaut, Pierre. "Comparison Between Lattice Boltzmann Method And Navier–stokes High Order Schemes For Computational Aeroacoustics." *Journal of Computational Physics* Vol. 228 No. 4 (2009): pp. 1056–1070. DOI 10.1016/j.jcp.2008.10.021.

[5] Chen, Shiyi and Doolen, Gary D. "Lattice Boltzmann Method For Fluid Flows." *Annual Review of Fluid Mechanics* Vol. 30 No. 1 (1998): pp. 329–364. DOI 10.1146/annurev.fluid.30.1.329.

[6] Krüger, Timm, Kusumaatmaja, Halim, Kuzmin, Alexandr, Shardt, Orest, Silva, Goncalo and Viggen, Erlend Magnus. *The Lattice Boltzmann Method: Principles And Practice*. Graduate Texts in Physics, Springer International Publishing (2017). DOI 10.1007/978-3-319-44649-3.

[7] Gourdain, Nicolas, L.Y.M., Gicquel and Morata, Elena. "RANS and LES for the Heat Transfer Prediction in Turbine Guide Vane." *Journal of Propulsion and Power* Vol. 28 (2012): pp. 423–433. DOI 10.2514/1.57717.

[8] Segui, Luis Miguel, Gicquel, Laurent, Duchaine, Florent and De Laborderie, Jérôme. "LES Of The LS89 Cascade: Influence Of Inflow Turbulence On The Flow Predictions." *Proceedings of 12th European Conference on Turbomachinery Fluid dynamics & Thermodynamics*. 2017. DOI 10.29008/ETC2017-159.

[9] Roy, Pamphile T., Segui, Luis Miguel, Jouhaud, Jean-Christophe and Gicquel, Laurent. "Resampling Strategies To Improve Surrogate Model-Based Uncertainty Quantification: Application To LES Of LS89." *International Journal for Numerical Methods in Fluids* Vol. 87 No. 12 (2018): pp. 607–627. DOI 10.1002/fld.4504.

[10] Troth, Luis Miguel Segui. "Multiphysics Coupled Simulations Of Gas Turbines." Ph.D. Thesis, Institut National Polytechnique de Toulouse - INPT. 2017.

[11] Kopriva, James, Gregory M. Laskowski and Laskowski, Gregory M. "Hybrid Large Eddy Simulations Of An Uncooled High Pressure Turbine Stator-Rotor Stage." *Proceedings of 12th European Conference on Turbomachinery Fluid dynamics & Thermodynamics*. 2017.

[12] Farag, G., Zhao, S., Coratger, T., Boivin, P., Chiavassa, G. and Sagaut, P. "A Pressure-Based Regularized Lattice-Boltzmann Method For The Simulation Of Compressible Flows." *Physics of Fluids* Vol. 32 No. 6 (2020). DOI 10.1063/5.0011839.

[13] Jacob, Jérôme, Malaspinas, Orestis and Sagaut, Pierre. "A New Hybrid Recursive Regularised Bhatnagar-Gross-Krook Collision Model For Lattice Boltzmann Method-Based Large Eddy Simulation." *Journal of Turbulence* Vol. 19 (2018): pp. 1–26. DOI 10.1080/14685248.2018.1540879.

[14] Guo, S, Feng, Y, Jacob, J, Renard, F and Sagaut, P. "An efficient lattice Boltzmann method for compressible aerodynamics on D3Q19 lattice." *Journal of Computational Physics* (2020): p. 109570.

[15] Zhao, S., Farag, G., Boivin, P. and Sagaut, P. "Toward Fully Conservative Hybrid Lattice Boltzmann Methods For Compressible Flows." *Physics of Fluids* Vol. 32 No. 12 (2020). DOI 10.1063/5.0033245.

[16] Wissocq, Gauthier, Coratger, T., Farag, G., Zhao, S., Boivin, Pierre and Sagaut, Pierre. "Restoring The Conservativity Of Characteristic-Based Segregated Models: Application To The Hybrid Lattice Boltzmann Method." *Physics of Fluids* Vol. 34 No. 4 (2022): pp. 046102–046102. DOI 10.1063/5.0083377.

[17] Coratger, T., Farag, G., Zhao, S., Boivin, P. and Sagaut, P. "Large-Eddy Lattice-Boltzmann Modeling Of Transonic Flows." *Physics of Fluids* Vol. 33 No. 11 (2021). DOI 10.1063/5.0064944.

[18] Farag, Gabriel, Coratger, Thomas, Wissocq, Gauthier, Zhao, Song, Boivin, Pierre and Sagaut, Pierre. "A unified hybrid lattice-Boltzmann method for compressible flows: bridging between pressure-based and density-based methods." *Physics of Fluids* Vol. 33 No. 8 (2021): p. 086101.

[19] Bhatnagar, P. L., Gross, E. P. and Krook, M. "A Model For Collision Processes In Gases. I. Small Amplitude Processes In Charged And Neutral One-Component Systems." *Physical Review* Vol. 94 No. 3 (1954): pp. 511–525. DOI 10.1103/PhysRev.94.511.

[20] Aristov, V.V. and Cheremisin, F.G. "The Conservative Splitting Method For Solving Boltzmann's Equation." *USSR Computational Mathematics and Mathematical Physics* Vol. 20 No. 1 (1980): pp. 208–225. DOI 10.1016/0041-5553(80)90074-9.

[21] Titarev, V.A. "Conservative Numerical Methods For Model Kinetic Equations." *Computers & Fluids* Vol. 36 No. 9 (2007): pp. 1446–1459. DOI 10.1016/j.compfluid.2007.01.009.

[22] Vreman, A. W. "An Eddy-Viscosity Subgrid-Scale Model For Turbulent Shear Flow: Algebraic Theory And Applications." *Physics of Fluids* Vol. 16 No. 10 (2004): pp. 3670–3681. DOI 10.1063/1.1785131.

[23] Smagorinsky, J. "General Circulation Experiments With The Primitive Equations: I. The Basic Experiment." *Monthly Weather Review* Vol. 91 No. 3 (1963): pp. 99–164. DOI 10.1175/1520-0493(1963)091<0099:GCEWTP>2.3.CO;2.

[24] Germano, Massimo, Piomelli, Ugo, Moin, Parviz and Cabot, William H. "A Dynamic Subgrid-Scale Eddy Viscosity Model." *Physics of Fluids A: Fluid Dynamics* Vol. 3 No. 7 (1991): pp. 1760–1765. DOI 10.1063/1.857955.

[25] Hewitt, Edwin and Hewitt, Robert E. "The Gibbs-Wilbraham Phenomenon: An Episode In Fourier Analysis." *Archive for History of Exact Sciences* Vol. 21 No. 2 (1979): pp. 129–160. DOI 10.1007/BF00330404.

[26] VonNeumann, J. and Richtmyer, R. D. "A Method For The Numerical Calculation Of Hydrodynamic Shocks." *Journal of Applied Physics* Vol. 21 No. 3 (1950): pp. 232–237. DOI 10.1063/1.1699639.

[27] Jameson, Antony. "Origins And Further Development Of The Jameson–schmidt–turkel Scheme." *AIAA Journal* Vol. 55 No. 5 (2017): pp. 1487–1510. DOI 10.2514/1.J055493.

[28] Temmerman, Lionel, Leschziner, Michael A., Mellen, Christopher P. and Fröhlich, Jochen. "Investigation Of Wall-Function Approximations And Subgrid-Scale Models In Large Eddy Simulation Of Separated Flow In A Channel With Streamwise Periodic Constrictions." *International Journal of Heat and Fluid Flow* Vol. 24 No. 2 (2003): pp. 157–180. DOI 10.1016/S0142-727X(02)00222-9.

[29] Lehmkuhl, O, Park, G I and Moin, P. "LES Of FLow Over The NASA Common Research Model With Near-Wall Modeling." Technical report no. Center for Turbulence Research. 2016.

[30] Wilhelm, S., Jacob, J. and Sagaut, P. "An Explicit Power-Law-Based Wall Model For Lattice Boltzmann Method–reynolds-Averaged Numerical Simulations Of The Flow Around Airfoils." *Physics of Fluids* Vol. 30 No. 6 (2018). DOI 10.1063/1.5031764.

[31] Wilhelm, Sylvia, Jacob, Jerome and Sagaut, Pierre. "A New Explicit Algebraic Wall Model For LES Of Turbulent Flows Under Adverse Pressure Gradient." *Flow, Turbulence and Combustion* Vol. 106 No. 1 (2021): pp. 1–35. DOI 10.1007/s10494-020-00181-7.

[32] Werner, H and Wengle, H. "Large-Eddy Simulation Of Thrbulent Flow Over And Around A Cube In A Plate Channel." *Turbulent Shear Flows 8*. Springer (1993).

[33] Malaspinas, O. and Sagaut, P. "Wall Model For Large-Eddy Simulation Based On The Lattice Boltzmann Method." *Journal of Computational Physics* Vol. 275 (2014): pp. 25–40. DOI 10.1016/j.jcp.2014.06.020.

[34] Kader, Ḅ.A. "Temperature And Concentration Profiles In Fully Turbulent Boundary Layers." *International Journal of Heat and Mass Transfer* Vol. 24 No. 9 (1981): pp. 1541–1544. DOI 10.1016/0017-9310(81)90220-9.

[35] Šarić, S., Basara, B. and Žunič, Z. "Advanced Near-Wall Modeling For Engine Heat Transfer." *International Journal of Heat and Fluid Flow* Vol. 63 (2017): pp. 205–211. DOI 10.1016/j.ijheatfluidflow.2016.06.019.

[36] Poinsot, T J and Lele, S K. "Boundary Conditions For Direct Simulations Of Compressible Viscous Flows." *JOURNAL OF COMPUTATIONAL PHYSICS* Vol. 101 (1992): pp. 104–129.

[37] Odier, Nicolas, Sanjosé, Marlène, Gicquel, Laurent, Poinsot, Thierry, Moreau, Stéphane and Duchaine, Florent. "A Characteristic Inlet Boundary Condition For Compressible, Turbulent, Multispecies Turbomachinery Flows." *Computers & Fluids* Vol. 178 (2019): pp. 41–55. DOI 10.1016/j.compfluid.2018.09.014.